SCIENTIFIC REPORTS

OPEN

SUBJECT AREAS:
NANOPARTICLES
COLLOIDS

Received
31 July 2014

Accepted
1 September 2014

Published
18 September 2014

Correspondence and requests for materials should be addressed to S.Z. (sjzhang@ipe.ac.cn) or J.Y. (jyang@ipe.ac.cn)

# Alloy $Cu_3Pt$ nanoframes through the structure evolution in Cu-Pt nanoparticles with a core-shell construction

Lin Han[1,2], Hui Liu[1], Penglei Cui[1], Zhijian Peng[2], Suojiang Zhang[1] & Jun Yang[1]

[1]State Key Laboratory of Multiphase Complex Systems, Institute of Process Engineering, Chinese Academy of Sciences, Beijing, China 100190, [2]School of Engineering and Technology, China University of Geosciences, Beijing, China 100083.

**Noble metal nanoparticles with hollow interiors and customizable shell compositions have immense potential for catalysis. Herein, we present an unique structure transformation phenomenon for the fabrication of alloy $Cu_3Pt$ nanoframes with polyhedral morphology. This strategy starts with the preparation of polyhedral Cu-Pt nanoparticles with a core-shell construction upon the anisotropic growth of Pt on multiply twinned Cu seed particles, which are subsequently transformed into alloy $Cu_3Pt$ nanoframes due to the Kirkendall effect between the Cu core and Pt shell. The as-prepared alloy $Cu_3Pt$ nanoframes possess the rhombic dodecahedral morphology of their core-shell parents after the structural evolution. In particular, the resulting alloy $Cu_3Pt$ nanoframes are more effective for oxygen reduction reaction but ineffective for methanol oxidation reaction in comparison with their original Cu-Pt core-shell precursors.**

Hollow structured noble metal nanoparticles with customizable shell compositions offer a promising approach to meet the high performance in catalysis[1–5]. The hollow interior increases the utilization of precious metals by diminishing the number of their buried nonfunctional atoms, and the control of the structure/morphology at atomic level provides an effective way to tailor the physical and chemical properties for a given application. A typical example is the Pt-Pd bimetallic nanoparticles with a hollow interior and porous dendritic shell, which are produced based on the selective chemical etching of Pd cores from dendritic Pt-on-Pd nanoparticles[6]. These Pt-Pd bimetallic nanoparticles show enhanced catalytic activity for methanol oxidation reaction compared to other Pt-based materials.

A large number of strategies based on sacrificial templates[7–10], galvanic replacement[11–15], oxygen etching[16,17], and Kirkendall effect[14,18] have been developed for the synthesis of hollow structured noble metal-based nanomaterials. Most recently, Stamenkovic and co-workers reported the synthesis of a highly active and durable class of electrocatalysts by exploiting the structural evolution of platinum-nickel (Pt-Ni) bimetallic nanocrystals[19]. They found the crystalline $PtNi_3$ polyhedra could be transformed into $Pt_3Ni$ nanoframes with the intact original $PtNi_3$ polyhedral morphology *via* the interior erosion in solution. After structural transformation, both the interior and exterior catalytic surfaces of the $Pt_3Ni$ nanoframes with open-framework structure, are composed of the nanosegregated Pt-skin structure, which exhibits superior oxygen reduction reaction (ORR) activity.

Independently, we also discovered an unique structural transformation phenomenon in Cu-Pt systems. As we will demonstrate in this work, the Cu-Pt nanoparticles with a core-shell construction could be transformed into alloy $Cu_3Pt$ nanoframes after a period of aging under ambient conditions in an nonpolar organic medium. This strategy was different from that reported by Jia, et al., where the polyhedral $PtCu_3$ alloy nanocrystals were prepared directly by a solvothermal protocol[20]. The as-prepared $Cu_3Pt$ nanoframes possess the rhombic dodecahedral morphology of their core-shell precursors after the structural evolution. In particular, the resulting alloy $Cu_3Pt$ nanoframes are more effective for ORR but ineffective for methanol oxidation reaction (MOR) in comparison with their core-shell Cu-Pt parents. This study offers a vivid example to demonstrate the tuning of the material properties by means of a structural tailoring. In addition, the mechanistic understanding of the structural transformation from core-shell to open structured alloy nanoparticles might be used toward the design and fabrication of other hetero-nanostructures for technological applications.

## Results and discussion

Fig. S1 in Supplementary Information (SI) shows the transmission electron microscopy (TEM) and high-resolution TEM (HRTEM) images of the as-prepared Cu nanoparticles, which were used as seeds in the subsequent

preparation of core-shell Cu-Pt nanoparticles. These Cu seeds were decahedral in morphology, nearly monodisperse, and had an average size of 18.8 nm. In addition, the twinned structure was also clearly observed in the TEM and HRTEM images of the as-prepared Cu seed particles.

Although the galvanic replacement between the Cu seed particles and $H_2PtCl_6$ precursors cannot be ruled out, under the experimental conditions, the reduction of $Pt^{4+}$ ions in the presence of Cu seeds does result in the formation of core-shell Cu-Pt nanoparticles instead of Pt nanoshells or CuPt alloys. The distribution of Cu and Pt in the bimetallic Cu-Pt nanoparticles was analyzed by energy dispersive X-ray spectroscopy (EDX) under the high-angle annular dark-field scanning TEM (HAADF-STEM) mode. Nanoscale element mapping of a single particle (SI Fig. $2c_0$) revealed that Cu was concentrated in the core region (SI Fig. $2c_1$ and $c_3$), while the Pt was distributed throughout the entire particle (SI Fig. $2c_2$ and $c_3$). SI Fig. $2b_0$ shows the TEM image of the bimetallic Cu-Pt product as-prepared by the successive reduction of $Cu(acac)_2$ and $H_2PtCl_6$ in oleylamine, which was found to consist of well dispersed nanoparticles with rhombic dodecahedral morphologies, as schematically illustrated along three representative zone axes (a and b series in SI Fig. S2), manifesting the high-yield output of the heterogeneous nanostructures (ca. 100%). The core-shell Cu-Pt polyhedra were uniform in size and had an overall average size of 26.6 nm. The X-ray diffraction (XRD) pattern showed two distinct metal phases, which could be indexed to the cubic Cu and Pt, respectively (SI Fig. 3a).

After keeping the core-shell Cu-Pt colloidal solution in toluene at ambient conditions for 3 weeks, they transformed into alloy $Cu_3Pt$ nanoframes. The distribution of Cu and Pt in the nanoframes was assayed by EDX analysis in the mode of HAADF-STEM. As evinced by the C series in Fig. 1, the elemental map of a representative nanoframe indicates that Cu and Pt are uniformly distributed throughout the entire particle, manifesting the formation of alloy structure. Additional evidences for the formation of alloy nanoframes were provided by line scanning analyses of a number of nanoframes in the high-angle annular dark-field STEM mode. As confirmed by the D and E series in Fig. 1, the Cu and Pt are also uniformly distributed throughout the nanoframe. The XRD pattern (SI Fig. 3b) shows the presence of a homogeneously mixed crystal lattice, which is well in accord with the cubic $Cu_3Pt$ alloy phase (JCPDS Card File 351358).

After structural evolution, the average size of alloy $Cu_3Pt$ nanoframes is 23.2 nm, smaller than that of their core-shell parents. However, the rhombic dodecahedral morphologies of core-shell Cu-Pt polyhedra are well inherited by the alloy $Cu_3Pt$ nanoframes, as collectively illustrated by the schemes (A series in Fig. 1) and TEM/HRTEM images (B series in Fig. 1). In addition, the HRTEM images in B series of Fig. 1 also indicate well-developed crystallinity. This is consistent with the XRD pattern of the final framed products, which shows a metallic face-centered cubic structure (SI Fig. S3b).

The final nanoframes were examined by X-ray photoelectron spectroscopy (XPS) to confirm their compositions. For the Cu component in the nanoframes, the Cu $2p_{3/2}$ signal could be deconvoluted into two peaks of different intensities at 932.3 eV and 933.8 eV (SI Fig. S4a), corresponding to the Cu at zerovalent and oxidation state, respectively[18]. The Pt 4f spectra can also be deconvoluted into two pairs of doublets. The more intense doublet (at 70.9 eV and 74.3 eV) corresponds to Pt metal, while the second and weaker doublet, with binding energies of ca. 1.4 eV higher than those of Pt metal, could be assigned to $Pt^{2+}$ as in PtO and $Pt(OH)_2$[21–23].

To elucidate the formation mechanism of the structural evolution from core-shell Cu-Pt nanoparticles to alloy $Cu_3Pt$ nanoframes, TEM was used to monitor the structure transformation process. The results are shown in Fig. 2. In comparison with the original core-shell Cu-Pt nanoparticles (Fig. $2A_1$ and $A_2$), after aging in toluene for 2 weeks, the shrinkage occurs for the Cu core, and the voids close to the edges or at the corners in the core-shell Cu-Pt polyhedra could be discerned by the brightness contrast between these sites and other regions in the TEM and HRTEM images (Fig. $2B_1$ and $B_2$). The particle size decreases while the rhombic dodecahedron morphology are practically unchanged, indicating that the structural transformation does not cause the collapse of the polyhedral structure. This structural evolution of core-shell Cu-Pt polyhedra continues until the Cu core in the core-shell nanoparticles is completely disappeared (3 weeks). The final product was alloy $Cu_3Pt$ nanoframes with an average size of 23.2 nm (Fig. $2C_1$ and $C_2$) and intact dodecahedron morphology. The completion of evolution was confirmed by extending the aging time to 4 weeks, where no further changes in the particle size and morphology were detected by TEM and HRTEM (Fig. $2D_1$ and $D_2$). The evolution process from core-shell Cu-Pt nanoparticles to alloy $Cu_3Pt$ nanoframes is also vividly illustrated using the schemes in Fig. 2 ($A_3$~$D_3$), which correspond to the TEM images collected at original stage, 2 weeks, 3 weeks, and 4 weeks, respectively.

The mechanism for the structural evolution from core-shell Cu-Pt polyhedra to alloy $Cu_3Pt$ nanoframes could be summarized by the scheme in Fig. 3. The twin structure of the Cu seeds, which accounted for many interesting electronic, optical, and catalytic properties[24–26], was essential for the development of the core-shell Cu-Pt nanoparticles with polyhedral morphology. The anisotropic growth of Pt on the surface of Cu seeds was natural due to the preferential growth of Pt at the high-energy twin boundary sites. With the increase of the Pt ratios, core-shell Cu-Pt nanoparticles with stellated or dendritic morphologies could be obtained, as shown in SI Fig. S5, further confirming the presence of anisotropic growth of Pt on the surface of multiply twinned seeds[27,28].

The Kirkendall effect in core-shell Cu-Pt polyhedra are proposed to account for the structural evolution from core-shell to nanoframes. In core-shell Cu-Pt nanoparticles with face-centered cubic structure, the smaller Cu atoms would diffuse into the Pt shell[29–32], generating vacancies to initiate the Kirkendall effect. Then, analogous to the Ag-Au system[14,33], in the diffusion intermetallic coupling form by Pt shell and Cu core in core-shell Cu-Pt polyhedra, the diffusion of copper in platinum is faster than that of platinum in copper due to the small size of cupper atoms (the atomic radii of copper and platinum are 145 and 177 pm, respectively). Therefore, the difference between fluxes of Cu and Pt will produce a net flux of metal atoms from the center to the surface, leading to the interior hollowing of the core-shell structure until the stable $Cu_3Pt$ alloy phase is formed. The mutual diffusion also interprets the size decrease of the final nanoframes in comparison with that of the original core-shell Cu-Pt polyhedra, although the diffusion of Pt is slower than that of Cu. In particular, the inhomogeneous distribution of Pt on the edges versus the surface in the core-shell Cu-Pt polyhedra due to the anisotropic growth of Pt on the surface of twinned Cu seeds results in the formation of nanoframes instead of alloy $Cu_3Pt$ polyhedra with continuous Pt surfaces and hollow interiors.

Addition of some element sulfur to the core-shell Cu-Pt colloidal solution in toluene can accelerate the structural transformation of core-shell Cu-Pt polyhedra. We initially aimed at finding a way to achieve the preparation of pure Pt nanoframes, and element sulfur was the candidate to eliminate the copper from the alloy $Cu_3Pt$ polyhedra through the formation of CuS. However, the heterodimers composed of CuS and hollow structured Pt with quasi-spherical shape (CuS-hPt) are the dominant product instead of Pt nanoframes, as shown by the TEM and HRTEM images in SI Fig. S5. The formation of CuS extracts the Cu component from the Pt shell, and hence leads to the loss of the polyhedral morphology.

In addition to the surface chemical compositions[34–36], the catalytic property of a bimetallic system is usually structure-dependent[37]. To demonstrate the effect of the different structures in bimetallic Cu-Pt systems on the catalytic properties, the alloy $Cu_3Pt$ nanoframes and their core-shell Cu-Pt precursors were loaded on Vulcan carbon support and examined for their electrocatalytic activities towards

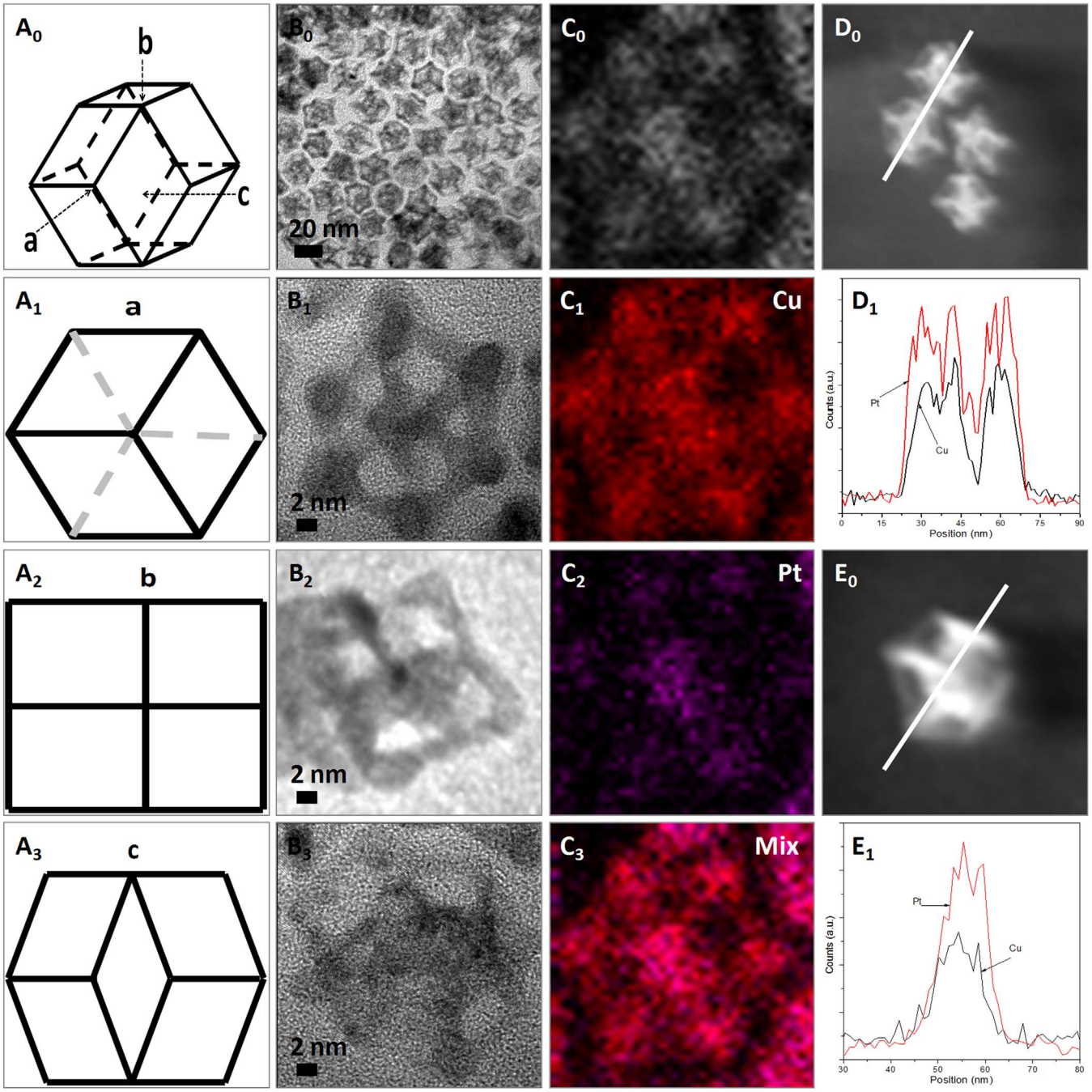


**Figure 1 | Characterization of final alloy $Cu_3Pt$ nanoframes.** Schematic illustrations (A series), corresponding TEM/HRTEM images (B series), element mapping (C series), and line-scanning analyses (D and E series) of the alloy $Cu_3Pt$ nanoframes evolved from core-shell Cu-Pt polyhedra in toluene under ambient conditions.

the room-temperature oxygen reduction reaction (ORR) and methanol oxidation reaction (MOR). As shown by the representative TEM and HRTEM images in SI Fig. S6, the core-shell Cu-Pt polyhedra and the resulting alloy $Cu_3Pt$ nanoframes after structure transformation were dispersed very well on the carbon support and the polyhedral morphology of the nanoparticles was intact.

Cyclic voltammograms of core-shell Cu-Pt/C and alloy $Cu_3Pt$/C in argon-purged 0.1 M $HClO_4$ at room temperature were used to obtain the electrochemical active surface areas (ECSAs) from the hydrogen adsorption/desorption regions (−0.2–0.1 V vs Ag/AgCl). As shown in Fig. 4A, the ECSAs normalized by the mass of Pt for core-shell Cu-Pt polyhedra and alloy $Cu_3Pt$ nanoframes are 45.6 $m^2\ g_{Pt}^{-1}$ and 30.2 $m^2\ g_{Pt}^{-1}$, respectively. The transformation from core-shell structure into open nanoframes may lead to the increase of ECSAs by releasing the inner surface of Pt shell, whereas the alloying with Cu during the structure evolution process would result in the decrease of ECSA due to the surface dilution of Pt by Cu component. These two effects might have offset each other, such that the ECSA of the alloy $Cu_3Pt$ nanoframes was smaller than that of core-shell Cu-Pt nanoparticles.

Fig. 4B showed the ORR polarization curves in the potential range of 0.9 to 0 V for alloy $Cu_3Pt$ nanoframes and their Cu-Pt core-shell parents in oxygen-saturated 0.1 M $HClO_4$ at room temperature. The half-wave potentials for the alloy $Cu_3Pt$ nanoframes and core-shell Cu-Pt polyhedra are 568 mV and 560 mV, respectively. The kinetic current density at half-wave potential of alloy $Cu_3Pt$ nanoframes is

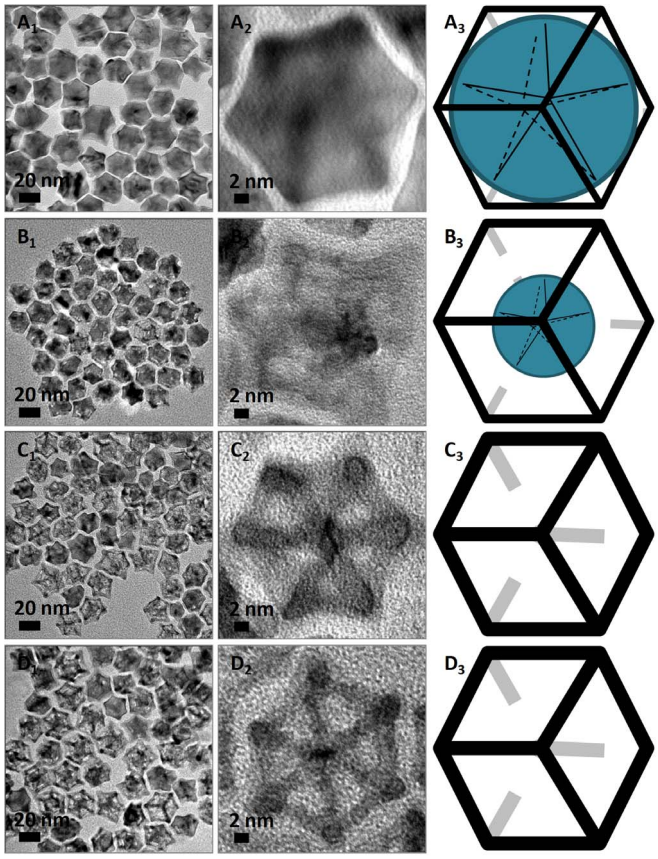


**Figure 2 | Core-shell Cu-Pt polyhedra observed at different stages during structure transformation.** TEM images ($A_1$~$D_1$), HRTEM images ($A_2$~$D_2$), and corresponding schematic illustrations ($A_3$~$D_3$) to show the core-shell Cu-Pt polyhedra aging in toluene for 0 week (A series), 2 weeks (B series), 3 weeks (C series), and 4 weeks (D series), respectively.

also higher than that of their Cu-Pt core-shell precursors. It has been noted that the half-wave potential for alloy $Cu_3Pt$ nanoframes is more positive than that of core-shell Cu-Pt nanoparticles, indicating that the $Cu_3Pt$ nanoframes have higher catalytic activity for ORR than that of core-shell Cu-Pt nanoparticles under the experimental conditions. The alloying of Pt with Cu during the structure evolution process provided some possible understanding of the enhanced ORR activity of alloy $Cu_3Pt$ nanoframes. Alloying Pt with transition metals

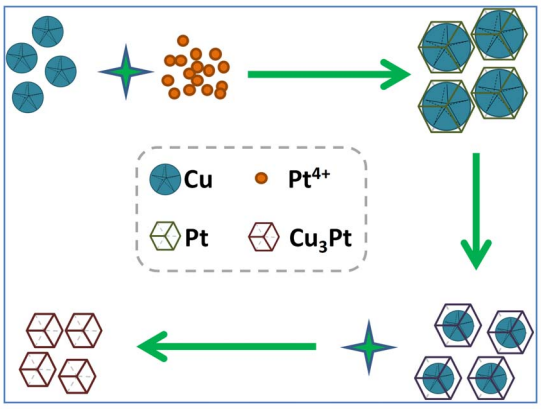


**Figure 3 | Mechanism accounting for the structure transformation.** Schematic illustration to demonstrate the mechanism for the structural evolution from core-shell Cu-Pt nanoparticles to alloy $Cu_3Pt$ nanoframes in toluene at ambient conditions.

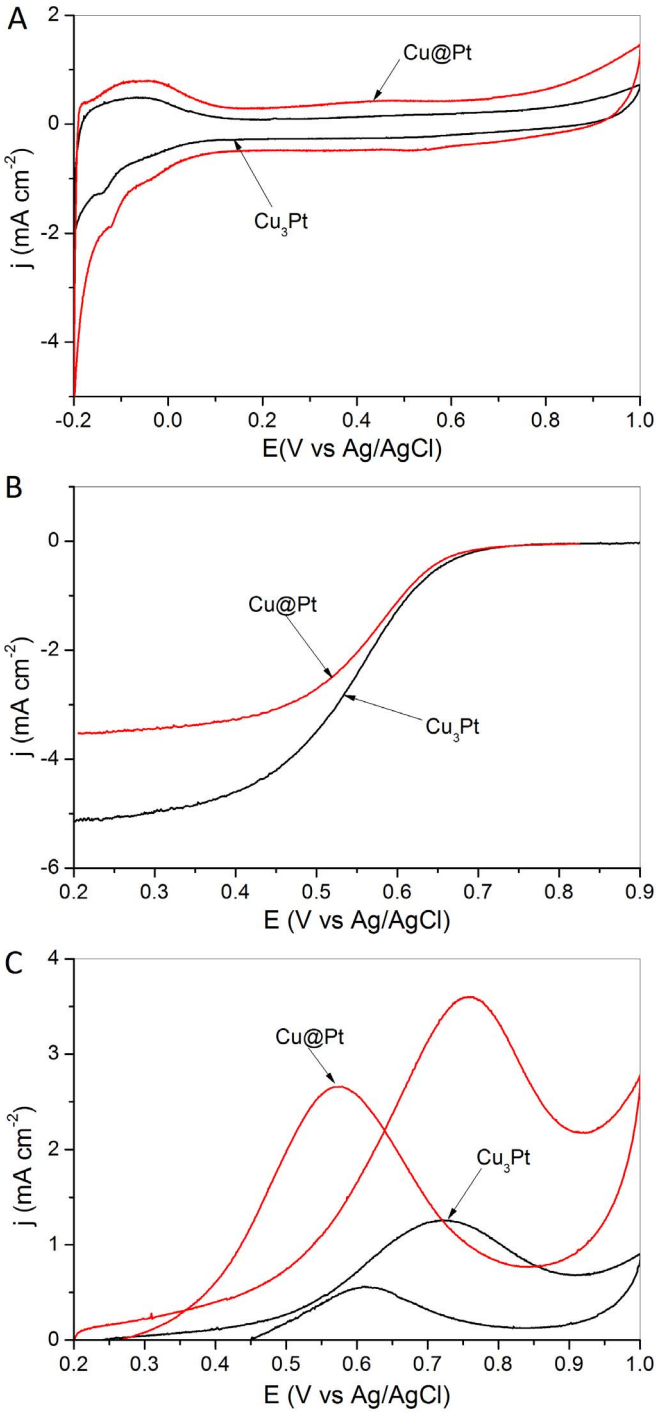


**Figure 4 | Electrochemical properties of Cu-Pt system with different structures.** (A) Cyclic voltammograms of core-shell Cu-Pt polyhedra and alloy $Cu_3Pt$ nanoframes in argon-purged $HClO_4$ (0.1 M) at room temperature, scan rate: 50 mV $s^{-1}$; (B) ORR polarization curves for core-shell Cu-Pt polyhedra and alloy $Cu_3Pt$ nanoframes recorded at room temperature in an $O_2$-saturated $HClO_4$ solution (0.1 M) at a sweep rate of 20 mV $s^{-1}$ and a rotating speed of 1600 rpm; (C) Cyclic voltammograms of core-shell Cu-Pt polyhedra and alloy $Cu_3Pt$ nanoframes in argon-purged $HClO_4$ (0.1 M) with 1 M methanol at 20 mV $s^{-1}$.

is usually an effective way to enhance the catalytic performance for ORR[5,38–42]. The effect of alloying is explainable in terms of the changes in Pt electronic structure[43,44]. For instance, the report by Watanabe and co-workers discussed the alloying effect of Fe, Ni or Co with Pt, where increase in ORR activity was observed. As Fe, Ni

and Co have more 5d vacancies than Pt, they would withdraw electrons from Pt and consequently increase the 5d vacancies in Pt. This increased the electron exchange between $O_2$ and Pt to promote oxygen reduction through enhanced $O_2$ adsorption[45].

On the other hand, the alloy $Cu_3Pt$ nanoframes were less active than their Cu-Pt core-shell parents for MOR. As exhibited in Fig. 4C, for alloy $Cu_3Pt$ nanoframes, the peak current densities associated with methanol oxidation in the forward and backward scans are only 1.25 and 0.68 mA $cm^{-2}$, respectively, much lower than those of core-shell Cu-Pt polyhedra (3.59 and 2.65 mA $cm^{-2}$, respectively). The high ratio of Cu in alloy $Cu_3Pt$ nanoframes, which would reduce the Pt surface sites available for occurrence of methanol oxidation reaction, may account for their poor activity for MOR. It has been generally accepted that methanol oxidation commences by methanol adsorption on multiple Pt sites (3-fold methanol adsorption sites, donated as $Pt_3$)[46]. For the alloy $Cu_3Pt$ nanoframes, the atomic mixing and uniform distribution of Cu and Pt on the surface may inhibit the adsorption of methanol, and therefore lead to negative effect on the catalytic activity for methanol oxidation.

In summary, alloy $Cu_3Pt$ nanoframes can be produced using Cu-Pt nanoparticles with a core-shell construction as precursors. This strategy was based on an unique structure evolution phenomenon in core-shell Cu-Pt nanoparticles with Cu residing in the core region. Upon the anisotropic growth of Pt on multiply twinned Cu seed particles, core-shell Cu-Pt nanoparticles with polyhedral morphology were first prepared, which were subsequently transformed into alloy $Cu_3Pt$ nanoframes due to the Kirkendall effect between the Cu core and Pt shell. The as-prepared alloy $Cu_3Pt$ nanoframes possess the rhombic dodecahedral morphology of their core-shell parents after the structural evolution. In particular, the resulting alloy $Cu_3Pt$ nanoframes are more effective for ORR but ineffective for methanol oxidation reaction (MOR) in comparison with the core-shell Cu-Pt nanoparticles. Although these materials cannot be used as practical electrocatalysts due to the low ratio of Pt on the surface, this study offers a vivid example to demonstrate the tuning of the material properties by means of a structural tailoring, and the structure evolution phenomenon may be extended to explore the alloy nanoframes composed of nobles other than Cu and Pt. This would result in some interesting examples with technological importance.

## Methods

**General materials.** Chloroplatinic acid hexahydrate ($H_2PtCl_6 \cdot 6H_2O$, ACS reagent, ≥37.5% Pt basis), copper(II) acetylacetonate ($Cu(acac)_2$, 97%), and oleylamine (70%, technical grade) from Sigma-Aldrich, element sulfur (S, ≥99.5%), aqueous $HClO_4$ solution (70%, ACS reagent), and Nafion 117 solution (5% in a mixture of lower aliphatic alcohols and water) from Aladdin Reagents, methanol (99%) and toluene (99.5%) from Beijing Chemical Works, and Vulcan XC-72 carbon powders (XC-72C, BET surface area = 250 $m^2 g^{-1}$ and average particle size = 40~50 nm) from Cabot Corporation, were used as received. All glassware and Teflon-coated magnetic stir bars were cleaned with *aqua regia*, followed by copious washing with de-ionized water before drying in an oven.

**Synthesis of Cu nanoseeds.** In a typical synthesis of Cu seed particles, 0.3 mmol (78.5 mg) of $Cu(acac)_2$ was dissolved in 10 mL of oleylamine placed in a three-necked flask equipped with a condenser and a stir bar. The solution was heated to 180°C under flowing $N_2$ and kept at this condition for 2 h for the reduction of $Cu^{2+}$ ions by oleylamine, which also served as the capping agent. No other reducing agent and stabilizer were used to form the Cu nanoparticles. After reaction, the Cu nanoparticles were purified by precipitation with methanol, followed by centrifugation and washing with methanol, and then re-dispersed in 10 mL of toluene.

**Synthesis of Cu-Pt nanopolyhedra with a core-shell construction.** For the synthesis of core-shell nanoparticles with a Cu core and a Pt shell, 0.3 mmol of $Cu(acac)_2$ was added to 10 mL of oleylamine in a three-necked flask fitted with a condenser and a stir bar. The solution was heated to 180°C and kept at this temperature under flowing $N_2$ for 2 h for the reduction of $Cu^{2+}$ ions by oleylamine. Then 0.1 mmol (41 mg) of $H_2PtCl_6$ was added swiftly, followed by increasing the temperature to 220°C and heating at that temperature for 2 h. After reaction, the core-shell Cu-Pt nanoparticles were purified by precipitation with methanol, centrifugation, washing with methanol, and re-dispersed in 20 mL of toluene.

**Evolution from core-shell Cu-Pt nanoparticles to alloy $Cu_3Pt$ nanoframes.** Typically, the structural evolution from core-shell Cu-Pt nanoparticles to alloy $Cu_3Pt$ nanoframes was observable by transmission electron microscopy (TEM) after aging the core-shell nanoparticles in toluene at room temperature for three weeks. Addition of element sulfur could accelerate the evolution process, affording heterogeneous nanodimers consisting of CuS and hollow structured Pt nanoparticles instead of $Cu_3Pt$ nanoframes.

**Particle characterizations.** Transmission electron microscopy (TEM), high resolution TEM (HRTEM), and scanning TEM (STEM) were performed on the JEOL JEM-2100 and FEI Tecnai $G^2$ F20 electron microscope operating at 200 kV with a supplied software for automated electron tomography. For the TEM measurements, a drop of the nanoparticle solution was dispensed onto a 3-mm carbon-coated copper grid. Excessive solution was removed by an absorbent paper, and the sample was dried under vacuum at room temperature. The mean particle size was obtained from a few randomly chosen areas in the TEM image containing approximately 100 nanoparticles each. An energy dispersive X-ray spectroscopy (EDX) analyzer attached to the TEM operating in the scanning transmission electron microscopy (STEM) mode was used to analyze the chemical compositions of the synthesized nanoparticles. X-ray photoelectron spectroscopy (XPS) was conducted on a VG ESCALAB MKII spectrometer. Powder X-ray diffraction (XRD) patterns were recorded on a Rigaku D/Max-3B diffractometer, using Cu Kα radiation (λ = 1.54056 Å). Samples for XPS and XRD analyses were concentrated from the toluene solution of nanoparticles to 0.5 mL using flowing $N_2$. 10 ml of methanol was then added to precipitate the nanoparticles, which were recovered by centrifugation, washed with methanol several times, and then dried at room temperature in vacuum.

**Electrochemical measurements.** Electrochemical measurements were carried out in a standard three-electrode cell connected to a Bio-logic VMP3 (with EC-lab software version 9.56) potentiostat. A leak-free Ag/AgCl (saturated with KCl) electrode was used as the reference electrode. The counter electrode was a platinum mesh (1×1 $cm^2$) attached to a platinum wire.

For the loading of the nanoparticles on Vulcan XC-72 carbon support, a calculated amount of carbon powder was added to the toluene solution of core-shell Cu-Pt nanoparticles and alloy $Cu_3Pt$ nanoframes. After stirring the mixture for 24 h, the nanoparticles/C (20 wt% Pt on carbon support) was collected by centrifugation, washed thrice with methanol, and then dried at room temperature in vacuum.

The working electrode was a thin layer of Nafion-impregnated catalyst cast on a vitreous carbon disk. This electrode was prepared by ultrasonically dispersing 10 mg of the nanoparticles/C in 10 mL of aqueous solution containing 4 mL of ethanol and 0.1 mL of Nafion solution. A calculated volume of the ink was dispensed onto the 5 mm of glassy carbon disk electrode to produce a nominal catalyst loading of 20 μg $cm^{-2}$ (Pt basis). The carbon electrode was then dried in a stream of warm air at 70°C for 1 h.

The room temperature cyclic voltammograms of core-shell Cu-Pt/C and alloy $Cu_3Pt$/C in argon-purged $HClO_4$ (0.1 M) were recorded between −0.2 V and 1 V at 50 mV $s^{-1}$ and used for the determination of electrochemically active surface area (ECSA) of Pt. The catalytic performance of core-shell Cu-Pt nanoparticles and alloy $Cu_3Pt$ nanoframes in room-temperature methanol oxidation reaction (MOR) was also measured by cyclic voltammetry. For these measurements the potential window of 0.2 V to 1 V was scanned at 20 mV $s^{-1}$ until a stable response was obtained. The electrolyte was methanol (1 M) in perchloric acid (0.1 M).

The catalytic performance of core-shell Cu-Pt nanoparticles and alloy $Cu_3Pt$ nanoframes in room-temperature oxygen reduction reaction (ORR) was evaluated in $HClO_4$ electrolyte solution (0.1 M) using a glass carbon rotating disk electrode (RDE) at a rotation speed of 1600 rpm. Negative-going linear sweep voltammograms were recorded from 0.9 V to 0 V at 20 mV $s^{-1}$ at room temperature in the presence of bubbling ultra-pure oxygen to maintain a saturated oxygen atmosphere near the working electrode. In the ORR polarization curve, the current density was normalized in reference to the ECSA to obtain the specific activities.


1. Kim, S.-W., Kim, M., Lee, W. Y. & Hyeon, T. Fabrication of hollow palladium spheres and their successful application to recyclable heterogeneous catalyst for Suzuki coupling reactions. *J. Am. Chem. Soc.* **124**, 7642–7643 (2002).
2. Liang, H.-P. *et al.* Pt hollow nanospheres: Facile synthesis and enhanced electrocatalysts. *Angew. Chem. Int. Ed.* **43**, 1540–1543 (2004).
3. Cheng, F., Ma, H., Li, Y. & Chen, J. $Ni_{1-x}Pt_x$ ($x = 0-0.12$) hollow spheres as catalysts for hydrogen generation from ammonia borane. *Inorg. Chem.* **46**, 788–794 (2007).
4. Bai, F. *et al.* Templated photocatalytic synthesis of well-defined platinum hollow nanostructures with enhanced catalytic performance for methanol oxidation. *Nano Lett.* **11**, 3759–3762 (2011).
5. Snyder, J., Livi, K. & Erlebacher, J. Oxygen reduction reaction performance of [MTBD][beti]-encapsulated nanoporous NiPt alloy nanoparticles. *Adv. Funct. Mater.* **23**, 5494–5501 (2013).
6. Wang, L. & Yamauchi, Y. Metallic nanocages: Synthesis of bimetallic Pt−Pd hollow nanoparticles with dendritic shells by selective chemical etching. *J. Am. Chem. Soc.* **135**, 16762–16765 (2013).
7. Zhang, D., Qi, L., Ma, J. & Cheng, H. Synthesis of submicrometer-sized hollow silver spheres in mixed polymer-surfactant solutions. *Adv. Mater.* **14**, 1499–1502 (2002).

8. Yang, J., Lee, J. Y., Too, H.-P. & Valiyaveettil, S. A bis(*p*-sulfonatophenyl)phenylphosphine- based synthesis of hollow Pt nanospheres. *J. Phys. Chem. B* **110**, 125–129 (2006).
9. Liu, H. *et al.* Hollow and cage-bell structured nanomaterials of noble metals. *J. Am. Chem. Soc.* **134**, 11602–11610 (2012).
10. Liu, H., Ye, F. & Yang, J. A universal and cost-effective approach to the synthesis of carbon-supported noble metal nanoparticles with hollow interiors. *Ind. Eng. Chem. Res.* **53**, 5925–5931 (2014).
11. Sun, Y., Mayers, B. T. & Xia, Y. Template-engaged replacement reaction: A one-step approach to the large-scale synthesis of metal nanostructures with hollow interiors. *Nano Lett.* **2**, 481–485 (2002).
12. Chen, H. M. *et al.* Hollow platinum spheres with nano-channels: Synthesis and enhanced catalysis for oxygen reduction. *J. Phys. Chem. C* **112**, 7522–7526 (2008).
13. Skrabalak, S. E. *et al.* Gold nanocages: Synthesis, properties, and applications. *Acc. Chem. Res.* **41**, 1587–1595 (2008).
14. González, E., Arbiol, J. & Puntes, V. F. Carving at the nanoscale: Sequential galvanic exchange and Kirkendall growth at room temperature. *Science* **334**, 1377–1380 (2011).
15. McEachran, M. *et al.* Ultrathin gold nanoframes through surfactant-free templating of faceted pentagonal silver nanoparticles. *J. Am. Chem. Soc.* **133**, 8066–8069 (2011).
16. Zheng, Y. *et al.* Oxidative etching and its role in manipulating the nucleation and growth of noble-metal nanocrystals. *Chem. Mater.* **26**, 22–33 (2014).
17. Xiong, Y. *et al.* Corrosion-based synthesis of single-crystal Pd nanoboxes and nanocages and their surface plasmon properties. *Angew. Chem. Int. Ed.* **44**, 7913–7917 (2005).
18. Wang, J. X. *et al.* Kirkendall effect and lattice contraction in nanocatalysts: A new strategy to enhance sustainable activity. *J. Am. Chem. Soc.* **133**, 13551–13557 (2011).
19. Chen, C. *et al.* Highly crystalline multimetallic nanoframes with three-dimensional electrocatalytic surfaces. *Science* **343**, 1339–1343 (2014).
20. Jia, Y. *et al.* Unique excavated rhombic dodecahedral $PtCu_3$ alloy nanocrystals constructed with ultrathin nanosheets of high-energy {110} facets. *J. Am. Chem. Soc.* **136**, 3748–3751 (2014).
21. Wagner, C. D. *et al.* [*NIST Standard Reference Database 20*], (Version 3.2, Web Version).
22. Yang, J., Lee, J. Y., Deivaraj, T. C. & Too, H.-P. An improved procedure for preparing smaller and nearly monodispersed thiol-stabilized platinum nanoparticles. *Langmuir* **19**, 10361–10365 (2003).
23. Yang, J., Deivaraj, T. C., Too, H.-P. & Lee, J. Y. An alternative phase-transfer method of preparing alkylamine-stabilized platinum nanoparticles. *J. Phys. Chem. B* **108**, 2181–2185 (2004).
24. Wang, Z. L. Transmission electron microscopy of shape-controlled nanocrystals and their assemblies. *J. Phys. Chem. B* **104**, 1153–1175 (2000).
25. Tang, Y. & Ouyang, M. Tailoring properties and functionalities of metal nanoparticles through crystallinity engineering. *Nature Mater.* **6**, 754–759 (2007).
26. Brodersen, S. H., Grønbjerg, U., Hvolbæk, B. & Schiøtz, J. Understanding the catalytic activity of gold nanoparticles through multi-scale simulations. *J. Catal.* **284**, 34–41 (2011).
27. Liu, H. *et al.* Stellated Ag-Pt bimetallic nanoparticles: An effective platform for catalytic activity tuning. *Sci. Rep.* **4**, 3969/1–3969/7 (2014).
28. Feng, Y., Liu, H. & Yang, J. Bimetallic nanodendrites via selective overgrowth of noble metals on multiply twinned Au seeds. *J. Mater. Chem. A* **2**, 6130–6137 (2014).
29. Wu, Y. *et al.* Defect-dominated shape recovery of nanocrystals: A new strategy for trimetallic catalysts. *J. Am. Chem. Soc.* **135**, 12220–12223 (2013).
30. Chen, W. *et al.* A seed-based diffusion route to monodisperse intermetallic CuAu nanocrystals. *Angew. Chem. Int. Ed.* **49**, 2917–2921 (2010).
31. Wang, C., Peng, S., Lacroix, L.-M. & Sun, S. Synthesis of high magnetic moment CoFe nanoparticles via interfacial diffusion in core/shell structured Co/Fe nanoparticles. *Nano Res.* **2**, 380–385 (2009).
32. Wang, C., Peng, S., Chan, R. & Sun, S. Synthesis of AuAg Alloy Nanoparticles from Core/Shell-Structured Ag/Au. *Small* **5**, 567–570 (2009).
33. Sun, Y. & Xia, Y. Mechanistic study on the replacement reaction between silver nanostructures and chloroauric acid in aqueous medium. *J. Am. Chem. Soc.* **126**, 3892–3901 (2004).
34. Yuan, X. *et al.* Development of Palladium Surface-Enriched Heteronuclear Au–Pd Nanoparticle Dehalogenation Catalysts in an Ionic Liquid. *Chem. Eur. J.* **19**, 1227–1234 (2013).
35. Zhang, J. *et al.* A series of NiM (M = Ru, Rh, and Pd) bimetallic catalysts for effective lignin hydrogenolysis in water. *ACS Catal.* **4**, 1574–1583 (2014).
36. Zhang, J. *et al.* Highly efficient, NiAu-catalyzed hydrogenolysis of lignin into phenolic chemicals. *Green Chem.* **16**, 2432–2437 (2014).
37. Liu, H. & Yang, J. Bimetallic Ag–hollow Pt heterodimers via insideout migration of Ag in core–shell Ag–Pt nanoparticles at elevated temperature. *J. Mater. Chem. A* **2**, 7075–7081 (2014).
38. Stamenkovic, V. R., Schmidt, T. J., Ross, N. P. & Marković, N. M. Surface composition effects in electrocatalysis: Kinetics of oxygen reduction on well-defined $Pt_3Ni$ and $Pt_3Co$ alloy surfaces. *J. Phys. Chem. B* **106**, 11970–11979 (2002).
39. Stamenkovic, V. R. *et al.* Improved oxygen reduction activity on $Pt_3Ni(111)$ via increased surface site availability. *Science* **315**, 493–497 (2007).
40. Stamenkovic, V. R. *et al.* Trends in electrocatalysis on extended and nanoscale Pt-bimetallic alloy surfaces. *Nat. Mater.* 6, 241–247 (2007).
41. Zhang, J., Yang, H., Fang, J. & Zou, S. Synthesis and oxygen reduction activity of shape-controlled $Pt_3Ni$ nanopolyhedra. *Nano Lett.* **10**, 638–644 (2010).
42. Cui, C. *et al.* Compositional segregation in shaped Pt alloy nanoparticles and their structural behaviour during electrocatalysis. *Nat. Mater.* **12**, 765–771 (2013).
43. Stamenkovic, V. R. *et al.* Changing the activity of electrocatalysts for oxygen reduction by tuning the surface electronic structure. *Angwe. Chem. Int. Ed.* **45**, 2897–2901 (2006).
44. Stamenkovic, V. R. *et al.* Effect of surface composition on electronic structure, stability, and electrocatalytic properties of Pt-transition metal alloys: Pt-skin versus Pt-skeleton surfaces. *J. Am. Chem. Soc.* **128**, 8813–8819 (2006).
45. Toda, T., Igarashi, H., Uchida, H. & Watanabe, M. Enhancement of the electroreduction of oxygen on Pt alloys with Fe, Ni, and Co. *J. Electrochem. Soc.* **146**, 3750–3756 (1999).
46. Gasteiger, H. A., Marković, N., Ross, P. N. & Cairns, E. J. Methanol electrooxidation on well-characterized platinum-ruthenium bulk alloys. *J. Phys. Chem.* **97**, 12020–12029 (1993).


## Acknowledgments

We thank Ms. Xiaohong Ma at Institute of Process Engineering, Chinese Academy of Sciences for her assistance in elemental mapping analyses of the core-shell nanomaterials in this study. Financial support from the 100 Talents Program of the Chinese Academy of Sciences, National Natural Science Foundation of China (No.: 21173226, 21376247), and State Key Laboratory of Multiphase Complex Systems, Institute of Process Engineering, Chinese Academy of Sciences (MPCS-2012-A-11) is gratefully acknowledged.

## Author contributions

L.H., H.L., P.C. and Z.P. performed the materials synthesis, characterization and electrochemical measurements. J.Y. and S.Z. supervised the project. J.Y. wrote the main manuscript text, and all authors participated in the review of the manuscript.

## Additional information

**Supplementary information** accompanies this paper at http://www.nature.com/scientificreports

**Competing financial interests:** The authors declare no competing financial interests.

**How to cite this article:** Han, L. *et al.* Alloy $Cu_3Pt$ nanoframes through the structure evolution in Cu-Pt nanoparticles with a core-shell construction. *Sci. Rep.* **4**, 6414; DOI:10.1038/srep06414 (2014).